Title

Double Perovskite Structure Induced by Co Addition to PbTiO3: Insights from DFT and Experimental Solid-State NMR Spectroscopy

Journal

Journal of Physical Chemistry C, 123(44)

ISSN

1932-7447

Authors

Mete, E
Odabaşl, S
Mao, H
et al.

Publication Date

2019-11-07

DOI

10.1021/acs.jpcc.9b06396

Peer reviewed

Double Perovskite Structure Induced by Co Addition to $PbTiO_3$: Insights From DFT and Experimental Solid State NMR Spectroscopy

Journal:	*The Journal of Physical Chemistry*
Manuscript ID	jp-2019-06396k.R2
Manuscript Type:	Article
Date Submitted by the Author:	n/a

Complete List of Authors:	Mete, Ersen; Balikesir Universitesi, Department of Physics Odabasi, Selda; Middle East Technical University, Chemical Engineering Mao, Haiyan; University of California Berkeley, Chemical and Biomolecular Engineering Chung, Tiffany; University of California Berkeley Ellialtioglu, Sinasi; TED University, Basic Sciences Reimer, Jeffrey; University of California Berkeley, Dept. of Chemical Engineering Gulseren, Oguz; Bilkent Universitesi, Department of Physics Uner, Deniz; Orta Dogu Teknik Universitesi, Chemical Engineering

Double Perovskite Structure Induced by Co Addition to $PbTiO_3$: Insights from DFT and Experimental Solid State NMR Spectroscopy

Ersen Mete,[*,†] Selda Odabaşı,[‡] Haiyan Mao,[¶,§] Tiffany Chung,[§] Şinasi Ellialtıoğlu,[‖] Jeffrey A. Reimer,[§] Oğuz Gülseren,[⊥] and Deniz Uner[*,‡]

†*Department of Physics, Balıkesir University, Balıkesir 10145, Turkey*

‡*Department of Chemical Engineering, Middle East Technical University, Ankara 06800, Turkey*

¶*College of Material Science & Engineering, Nanjing Forestry University, 159 Longran Road Naijing 210037, China*

§*Chemical and Biomolecular Engineering, University of California Berkeley, CA 94720, USA*

‖*Basic Sciences, TED University, Kolej, Ankara 06420, Turkey*

⊥*Department of Physics, Bilkent University, Ankara 06800, Turkey*

E-mail: emete@balikesir.edu.tr; uner@metu.edu.tr

Abstract

The effects of Co addition on the chemical and electronic structure of $PbTiO_3$ were explored both by theory and through experiment. Cobalt was incorporated into $PbTiO_3$ during sol gel process with the XRD data of the resulting compounds confirming a perovskite structure for the pure samples. The XRD lines broadened and showed emerging cubic structure features as the Co incorporation increased. The changes in the XRD pattern were interpreted as double perovskite structure formation. ^{207}Pb NMR measurements revealed a growing isotropic component in the presence of Co. Consistent with the experiments, DFT calculated chemical-shift values corroborate isotropic coordination of Pb, suggesting the formation of cubic Pb_2CoTiO_6 domains in the prepared samples. Hybrid functional first-principles calculations indicate formation of Pb_2CoTiO_6 with cubic structure and confirms that Co addition can decrease oxygen binding energy significantly. Experimental UV-Vis spectroscopy results indicate that upon addition of Co, the band gap is shifted towards visible wavelengths as confirmed by energy band and absorption spectra calculations. The oxygen binding energies were determined by temperature programmed reduction (TPR) measurements. Upon addition of Co, TPR lines shifted to lower temperatures and new features appeared in the TPR patterns. This shift was interpreted as weakening of oxygen cobalt bond strength. The change in the electronic structure by the alterations of oxygen vacancy formation energy and bond lengths upon Co insertion are determined by DFT calculations.

Introduction

The $PbTiO_3$ perovskite family of materials have a diverse range of applications.[1,2] Their chemical and electronic structure coupled with the tunability of the band gap and polarizability make these materials attractive.[3–6] The ease with which they create oxygen vacancies not only diversifies their electronic properties, but also makes them attractive chemical compounds triggering redox reactions.[7] Furthermore, the band gap of these compounds can also be easily tuned by doping, resulting in tunable features such as band gaps.[8–11] For example,

chemically doped $PbTiO_3$ structures are utilized for hydrogen production by photocatalytic[12] and photoelectrochemical[13] cells as anode materials. Our selection of $PbTiO_3$ mainly stems from two reasons. First, $PbTiO_3$ is itself a good visible light photocatalyst, thus acting as an oxidizer, and its structural and electronic properties are well known. Second, together with the oxides of Co, PbO_x can exchange all of its oxygen at relatively low temperatures.[14] These properties become important when considering the storage of solar energy in the chemical bonds. Widespread availability of such technologies is crucial for off-grid localized energy production including fuel cells as well as for space applications. Perovskites emerge as potentially promising candidates[15] based on a thermodynamic analysis of oxygen vacancy formation.[16,17]

We report a fundamental study about Co added $PbTiO_3$ (PCTO) materials with particular attention to solid-state ^{207}Pb NMR spectroscopy, where the effect of Co is reflected in the chemical shifts and the lineshapes of the signal. Magnetic resonance methods are versatile tools for simultaneously elucidating the geometric structure along with the electronic properties.[18,19] Density functional theory (DFT) is used[20,21] to determine the source of the NMR shifts as well as the changes in the electronic structures and in the UV–Vis spectra of Co-doped $PbTiO_3$.

Methodology

Preparation of the Materials

Lead (II) Acetate Trihydrate (LAT) (extra pure, MERCK), titanium (IV) isopropoxide (97%, Sigma-Aldrich) (TIP), Cobalt (II) Acetate Tetrahydrate (pure, MERCK) (CAT) were used as precursors and citric acid (99%, Aldrich) (CA) as gelation agent. LAT was dissolved in the minimum amount of acetic acid glacial and 50% by volume mixture of ethanol-acetic and acid glacial was used to dissolve TIP and ethanol is used to dissolve citric acid. The molar ratio of LAT, TIP and CA was (1:1:2), respectively. The solution containing TIP

was added to the solution containing LAT under vigorously stirring. As soon as CA-ethanol solution was introduced to the mixture, a white gel was formed. The gel was kept under vigorous stirring and later it was transferred on the hot plate. A white solidified gel was obtained as a result. Afterwards, the white solidified gel was placed in the oven and kept there overnight at 100 °C to remove volatile organic solvents and water. The white powder was heated to 650 °C at a rate of 5 °C/min for calcination and kept at that temperature for 3 hours. After calcination, a yellow powder was obtained. The same procedure was applied to prepare cobalt containing samples with the following modifications. Appropriate amount of Cobalt (II) Acetate Tetrahydrate (pure, MERCK) (CAT) was dissolved in the LAT-acetic acid solution. The molar ratios of LAT, CAT, TIP and CA were adjusted to attain the desired x = Co/(Pb+Co) to prepare PCTO. After calcination, a gray powder was obtained for $x = 0.875$, a green powder was obtained for $x = 0.75$ and a green powder was obtained for $x = 0.5$.

Characterization

XRD analysis was used to determine phase identification and the crystallinity of $PbTiO_3$ and PCTO samples. Analyses were performed in Philips PW 1840 Compact X-ray Diffractometer equipment (-30kV, 24mA- with Cu Kα radiation). The scattering angle was from 5 to 90°. The compositions of synthesized perovskites are analyzed by using Perkin Elmer Optima 4300DV inductively coupled plasma–optical emission spectrometry.

Solid-State NMR Spectroscopy ^{207}Pb static SS-NMR spectra were collected on a 11.7 T magnet at a ^{207}Pb frequency of 104.53 MHz. A Bruker narrow bore H/C/N probe was used. A ^{207}Pb 90° pulse of 3.3 s was measured in solid $Pb(NO_3)_2$. $Pb(NO_3)_2$ was used as a secondary chemical shift reference with the left horn of powder pattern was set to 3490 ppm (relative to Me_4Pb). ^{207}Pb Hahn echo experiments were performed with an interpulse delay of 20 s. The relaxation delay was used as 60 s for $PbTiO_3$, 30 s for PCTO samples. All the NMR measurements were obtained at room temperature ($\approx$ 25 °C).

UV-Vis spectroscopy analysis was done in Shimadzu UV-2450 equipment. The ab-

sorbance data was measured between 200 nm and 800 nm. Barium sulfate was used as reference sample.

Micromeritics Chemisorb 2720 equipment was used for TP_X analyses. Temperature programmed reduction (TPR) experiments were conducted to measure the reducibility of samples. The composition of the effluent gases are tracked by a thermal conductivity detector (TCD). Before letting the gas flow through the system, the samples are placed between quartz wool in the U-shaped quartz reactor and the quartz reactor is placed in a furnace which can be heated up to 1100 °C. A cold trap, a mixture of ice, water, and isopropyl alcohol is used to remove condensables, particularly water vapor from the product stream before the analysis. The final temperature, heating rate and stand by time at final temperature are fixed using TP_X controller.

Computational Details

Density functional calculations have been performed with the Vienna ab-initio simulation package (VASP)[22] using the projector-augmented wave (PAW) method.[23,24] The single particle states have been expanded in plane waves up to a kinetic energy cutoff value of 400 eV. The exchange and correlation effects were taken into account using the modern hybrid Heyd–Scuseria–Ernzerhof (HSE)[25–27] scheme.

The standard density functionals are known to be insufficient for describing the perovskite materials.[28] Estimation of their structural and vibrational properties improves with meta-GGA functionals.[29,30] In the absence of a proper self-interaction cancellation between the Hartree and exchange terms leads to a significant band gap underestimation. Hybrid approaches have been proposed to improve the description of electronic structures over usual GGA functionals.[31] The screened Coulomb hybrid density functional, HSE,[25–27] partially incorporates the exact Fock exchange and the PBE[32] exchange energies. The HSE[25–27] correlation energy and the long-range (LR) part of the exchange energy is taken from the PBE[32] functional. The short-range (SR) part of the exchange energy is mixed with the PBE

counterpart using η as the mixing coefficient[33] as,

$$E_{\mathrm{X}}^{\mathrm{HSE}} = \eta E_{\mathrm{X}}^{\mathrm{HF,SR}}(\omega) + (1-\eta)E_{\mathrm{X}}^{\mathrm{PBE,SR}}(\omega) + E_{\mathrm{X}}^{\mathrm{PBE,LR}}(\omega)$$

where ω is the range separation parameter.[25–27] We employed the HSE12s[34] functional which optimizes these parameters to reduce the Fock exchange length scale without decreasing the overall accuracy of HSE06[26] significantly. This range separated hybrid density functional approach improves the band gap related properties over the standard exchange–correlation (XC) schemes and offers a better description of localized d states of transition metals. In particular, the position and dispersion of possible Co-driven gap states are important for Co-doped $PbTiO_3$. Recently, the hybrid DFT approach has been successfully employed to get the electronic structures of perovskite oxides.[35,36]

In order to determine the structure of the perovskite with Co, a (2×2×2) supercell was constructed from the bulk unit cell of $PbTiO_3$. Then we traced possible interstitial and substitutional Co incorporation models with various Co/(Pb+Co) ratios. Geometry optimization of Co involvement ended up with cubic symmetry only for a supercell which contains 4 Ti and 4 Co atoms in an alternating order. All other Co incorporation models lead to tetragonal symmetry. The Brillouin zone integrations have been carried out over a Γ-centered 8×8×8 k-point grid. Both the cell volume and the atomic positions were fully optimized self-consistently until the Hellmann–Feynman forces on each ion in each cartesian direction was less than 0.01 eV/Å.

The DFT–NMR calculations were performed based on the linear response GIPAW method.[37–39] The chemical shift tensor component values at a nuclear site at $\mathbf{R}$ were determined from,

$$\delta_{ij}(\mathbf{R}) = \frac{\partial B_i^{\mathrm{ind}}(\mathbf{R})}{\partial B_j^{\mathrm{ext}}}$$

where i and j are the cartesian indices, B^{ext} is an applied DC external magnetic field, and

$B^{\mathrm{ind}}(\mathbf{R})$ is the induced magnetic field at $\mathbf{R}$. Then a proper referencing to TML is done using

$$\delta_{\mathrm{iso}}^{\mathrm{calc.}}(^{207}\mathrm{Pb}) = \delta_{\mathrm{iso}}^{\mathrm{ref}} - \delta_{\mathrm{iso}}^{\mathrm{PCTO}} \quad \text{(all in ppm)},$$

where a single TML molecule is considered in a large computational cell.

Technically, NMR chemical shift calculations require a higher cutoff value than the usual. We set it to 600 eV. A more stringent tolerance is also needed to stop the self-consistent loop. We used a value of 10^{-10} eV for the difference of the total energies between the electronic iterations.

Results & Discussion

Structure Analysis

Structure of the synthesized samples of PTO and PCTO with Co/(Pb+Co) ratios $x = 0.125$, 0.25,and 0.5 were determined using XRD analysis (See Fig. 1). Upon Co addition, the peaks corresponding to (101) and (110), (201) and (210), (112) and (211) broaden and merge. As Co content increases in the samples, cubic planes become dominant to the detriment of tetragonality. In addition, as cobalt content increased, intensity of the peaks decreased, suggesting the decrease of the crystal grain size as cobalt content increased.

The tetragonal phase of $PbTiO_3$ is shown in Fig. 2a. Since, the experimental XRD data indicate the presence of a cubic phase in the Co added $PbTiO_3$. We checked all possible cubic structures including substitutional (for Pb and/or Ti) and interstitial dopings. The only consistent cubic structure obtained is for Pb_2CoTiO_6 as shown in Fig. 2b.

We performed geometry optimization calculations without imposing space group symmetry and allowed a full volume relaxation by lifting any restriction on the lattice translation vectors. At 325 K, $PbTiO_3$ forms the tetragonal phase having $P4mm$ space group symmetry

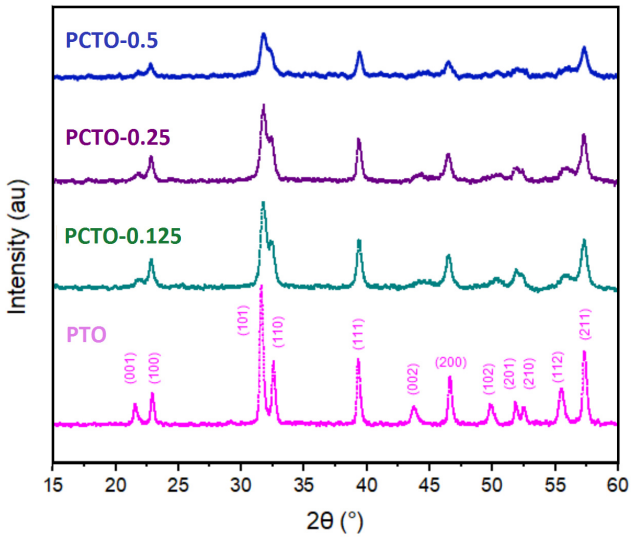

Figure 1: (color on-line) XRD patterns of $PbTiO_3$ and PCTO with various Co/(Pb+Co) ratios ($x = 0.125$, 0.25, and 0.5).

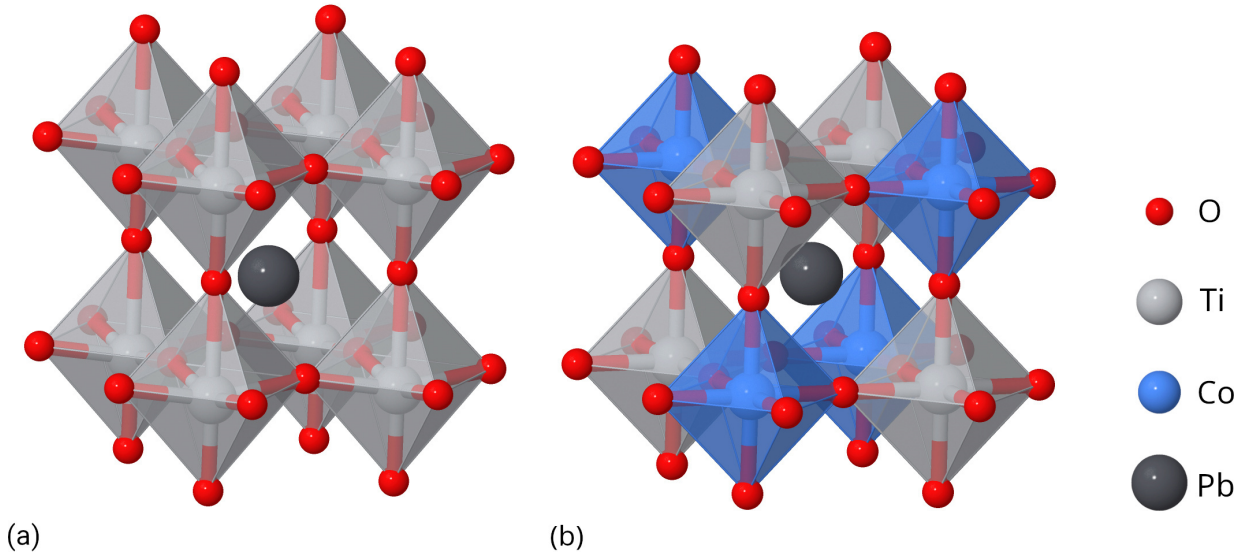

Figure 2: (color on-line) Schematic (a) tetragonal $PbTiO_3$ and (b) cubic Pb_2CoTiO_6 structures.

with cell parameters $a = 3.899$ Å and $c = 4.138$ Å.[41] The lattice constants were found as $a = 3.864$ Å and $c = 4.045$ Å using the HSE12s functional. The largest deviation from the experimental values comes from the c parameter which is ∼2.2%. This is known as the super-tetragonality problem of HSE functional which is based on local density approximation (LDA). A recent theoretical study reported similar values with reasonable agreement using

Table 1: Atomic positions of tetragonal ($P4mm$) $PbTiO_3$ and cubic ($Fm\bar{3}m$) Pb_2CoTiO_6. DFT results were obtained using the HSE12s XC-functional.

$PbTiO_3$							Pb_2CoTiO_6				
Atom	x*	y*	z*	x	y	z	Atom	x	y	z	Site
Pb	0.000	0.000	0.000	0.000	0.000	0.000	Pb	1/4	1/4	1/4	8c
Ti	0.500	0.500	0.530	0.500	0.500	0.535	Co	1/2	1/2	1/2	4b
O1	0.500	0.500	0.074	0.500	0.500	0.087	Ti	0	0	0	4a
O2	0.500	0.000	0.641	0.500	0.000	0.610	O	0.2563(4)	0.000	0.000	24e

* Experimental values for $PbTiO_3$ are taken from Ref.[40] .

the HSE06 XC functional.[30] The atomic coordinates are presented in Table 1.

The change in the XRD peaks as the Co content increases in the samples indicates the presence of a cubic phase in relation to Co. In addition, SS-NMR measurements reveal isotropic chemical environment for Pb atoms in the PCTO materials. Preparation process of Co added $PbTiO_3$ leads to formation of Pb_2CoTiO_6 domains which involve TiO_6 and CoO_6 octahedra as shown in Fig. 2b. The double perovskite has a cubic $Fm\bar{3}m$ symmetry ($a = 7.68$ Å) where Co and Ti sit at the corners of the cube in an alternating manner. In this structure, a Pb atom, being at the center, is 12-fold-coordinated with the nearest oxygens which lie at the mid-points of the edges of the cube.

NMR Spectroscopy

Hahn-echo spectra from pure $PbTiO_3$ (red, not aged), $PbTiO_3$ (blue, aged one month at 280 K) and $PbTiO_3$ with trace amount of cobalt, also aged one month at 280 K (green) are shown in Fig. 3. NMR spectra of the pure compounds are consistent with the reports from the literature[42] while cobalt doped sample reveals a broadening at the left horn and a ∼100 ppm shift to lower frequencies.

The NMR spectra of Co modified $PbTiO_3$ are shown in Fig. 4. When high amounts of cobalt were introduced in the sample at the percent levels to replace Pb and/or Ti atoms

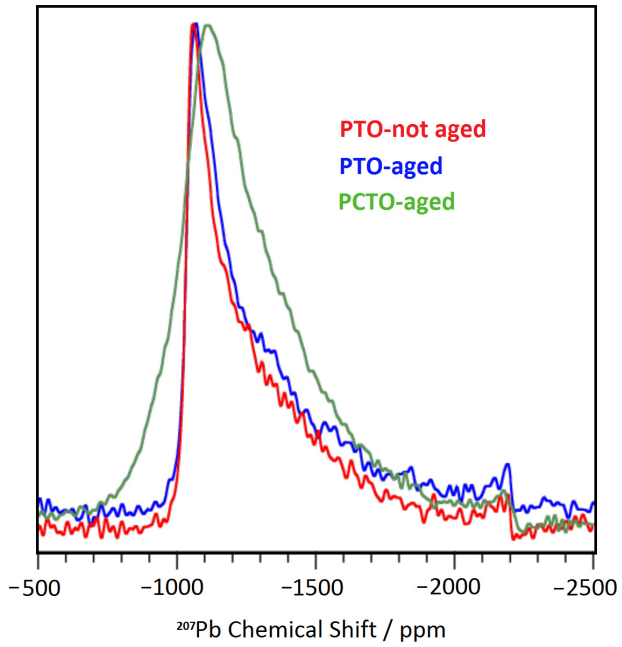

Figure 3: (color on-line) The effect of aging during sol gel and addition of a trace amount of Co (PCTO) on the NMR lineshape of $^{207}PbTiO_3$.

in the perovskite lattice, the NMR lineshape evolved into a broad, featureless peak centered around the horn of the pure $PbTiO_3$ spectrum. At the intended 50% replacement of the Pb atoms with Co, the intensity diminished completely, due to both broadening and diminished amount of Pb nuclei in the sample. The total intensities of the other Co containing samples were consistent with the intensity of the pure compound, indicating that at $\leq$25% Co, most of the nuclei were accessible by NMR.

NMR linesphape simulations shown in Fig. 5 reveal superposition of two features. One feature is the unperturbed $PbTiO_3$ lineshape, the second feature is a broad symmetric isotropic peak. These ^{207}Pb NMR data suggest coexistence of Pb in two different local phases in the samples. The chemical shift anisotropy (CSA) tensor component estimations of lineshape simulations are consolidated in Table 2.

This analysis of NMR spectra suggests an isotropic structure, so we searched bonding scenarios for Pb thoroughly. We considered all possible models for Co inclusion to $PbTiO_3$ lattice such as substitutional (for Pb and/or Ti) and interstitial dopings. The only probable

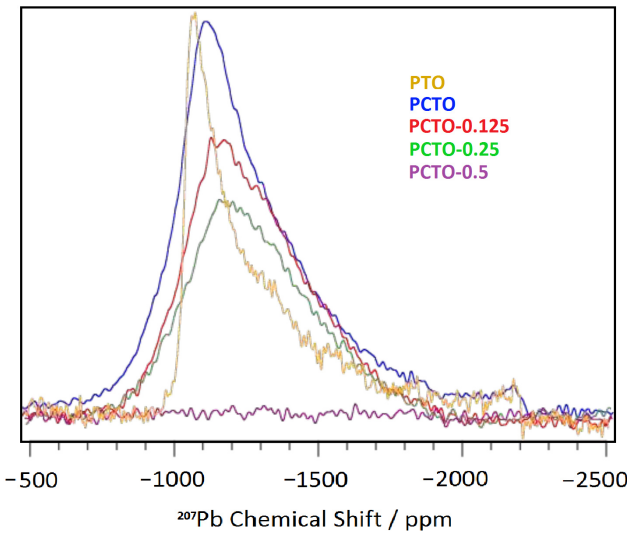

Figure 4: (color on-line) The effect of Co addition on the NMR lineshape of $^{207}PbTiO_3$.

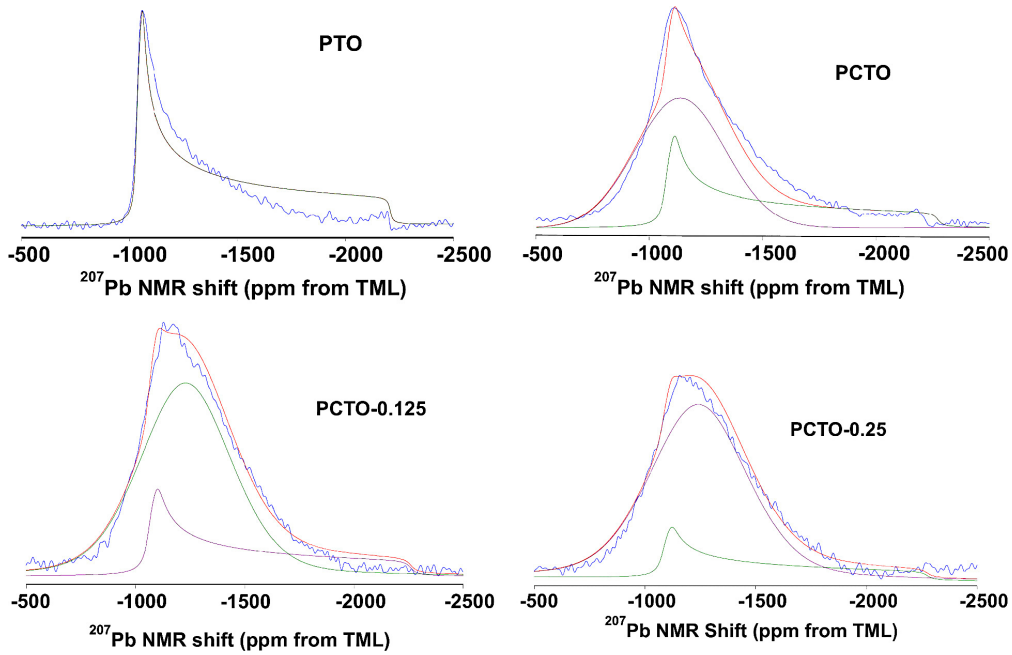

Figure 5: (color on-line) NMR lineshape simulations.

geometry is found as Pb_2CoTiO_6 which forms in a cubic structure where oxygen and Pb coordination is isotropic.

The DFT calculations are used to elucidate the role of Co dopants on the chemical shift of ^{207}Pb. The local chemical environments are reflected in the diagonal components of chemical shift anisotropy tensor estimated from DFT, as compiled in Table 3. The left horn of the

Table 2: DM Fitting, Chemical shift anisotropy+Gaus/Lor

Compound	δ_{xx}	δ_{yy}	δ_{zz}	δ_{iso}	δ_{aniso}	η	Span
PTO	−1032.50	−1059.59	−2207.02	−1433.04	−773.98	0.0063	1174.52
PCTO-trace	−1052.88	−1076.48	−2244.76	−1458.04	−786.72	0.0054	1191.87
PCTO-0.125	−1124.20	−1165.90	−2270.52	−1520.21	−750.33	0.0091	1120.59
PCTO-0.25	−1138.05	−1150.75	−2252.80	−1513.84	−738.88	0.0028	1101.05

Table 3: Chemical shift anisotropy values (in ppm) estimated from DFT in tetragonal $PbTiO_3$ and in cubic Pb_2CoTiO_6.

model structure	δ_{xx}	δ_{yy}	δ_{zz}
$PbTiO_3$	−1032	−1032	−1538
Pb_2CoTiO_6	−1148	−1148	−1148

^{207}Pb NMR spectrum in $PbTiO_3$ is a result of symmetry characteristics of Pb–O bonding (mainly two types of Pb–O bonds with lengths 2.75 Å and 3.09 Å) in pure tetragonal $PbTiO_3$. We surmised that as Co is mixed into the sample oxygen octahedra form with Co and/or Ti at the center which leads to formation of a cubic Pb_2CoTiO_6 double perovskite structure. In this structure Pb–O coordination is isotropic. Therefore, Pb–O bonds become similar in length and in covalency. Since the valence electron distribution around each of the Pb nucleus gets affected by Co incorporation, their shielding responses to an external magnetic field show the isotropic nature this cubic structure. Although the relativistic effects are not included in the GIPAW implementation of VASP, the DFT calculations yield ^{207}Pb NMR features consistent with the experimental spectra.

Oxygen Bonds

The effect of a single oxygen vacancy formation on the $PbTiO_3$ lattice structure is considered using a (2×2×2) supercell containing 40 atoms. In the absence of an oxygen atom both from the PbO layer (O1) and from the TiO_2 layer (O2), small lattice distortions occur and remain

in the local environment. The oxygen vacancy formation energy can be formulated as

$$E_{\mathrm{f}} = E_{\mathrm{PCTO}} - E_{\mathrm{PCTO'}} - E_{\mathrm{O}}$$

where E_{PCTO} and $E_{\mathrm{PCTO'}}$ are the total cell energies of $PbTiO_3$ without and with an oxygen defect, respectively. E_{O} is the energy of an oxygen atom in the O_2 molecule for which the calculation procedure is adopted from Ref.[43] The energy required to remove one oxygen atom from the undoped bulk system is as large as 5.28 eV per O1 and 5.14 eV per O2. In Pb_2CoTiO_6 structure, the chemical bonding characteristics of all oxygens are equal and the vacancy formation energy is 3.12 eV. Therefore, Co addition to $PbTiO_3$ leads to a significant drop in the oxygen vacancy formation energy.

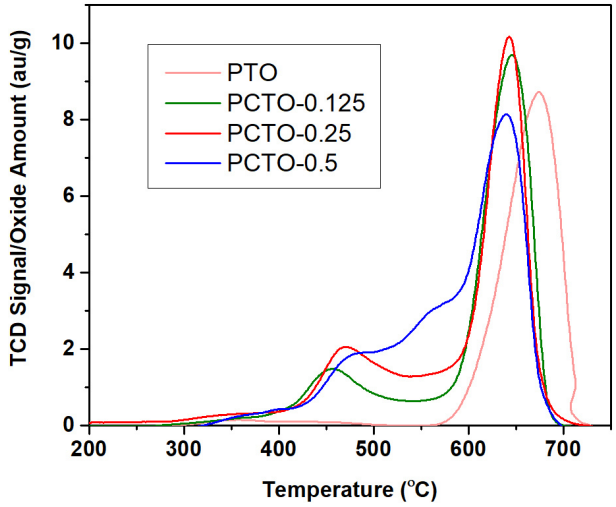

Figure 6: (color on-line) TPR profiles of perovskites.

Table 4: TPR peak positions of synthesized perovskites

Sample	Peak Positions (°C)	Additional Peaks (°C)
PTO	675	–
PCTO-0.125	646	455
PCTO-0.25	643	158, 469
PCTO-0.5	640	400, 478, 558

Temperature programmed reduction (TPR) profiles of the perovskites are consolidated

in Fig. 6. It is clearly seen that the addition of Co decreased the reduction temperature of the material, indicative of weaker oxygen bonds in these structures. The peak temperatures were compiled in Table 4 for comparison. Here, the 675 °C peak can be observed for all perovskites. As Co is introduced, peak position shifts to 646 °C which indicates a weaker oxygen bond energy in the structure. Further addition of Co does not significantly influence the peak position.

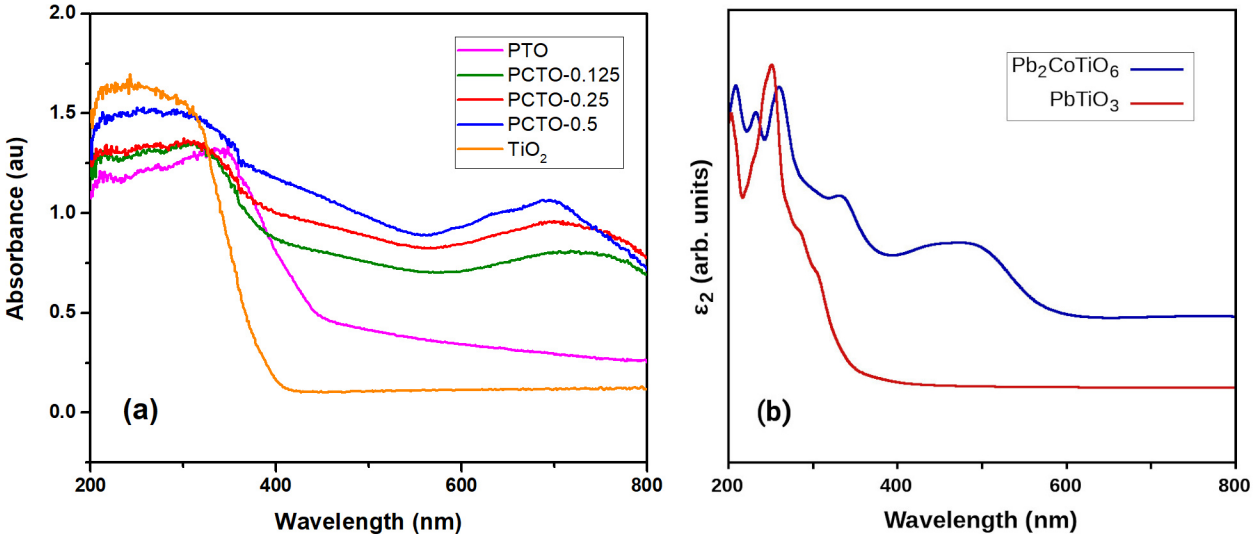

Figure 7: (color on-line) (a) UV-Visible Diffuse Reflectance Spectra of TiO_2, pure and Co added $PbTiO_3$. (b) THe imaginary part of the dielectric matrix of $PbTiO_3$ and Pb_2CoTiO_6 calculated using the HSE12s XC-functional.

Electronic structure

In Fig. 7a, experimentally measured UV-Visible diffuse reflectance spectra is shown. All synthesized perovskites and TiO_2 had strong absorption between 200 nm–400 nm. For $PbTiO_3$, absorption edge is larger than the absorption edge of TiO_2. The result conforms with the literature.[44,45] The peak around 650 nm–800 nm for Co-doped samples was originated from Co^{4+} species. Dai *et al.* showed that Co_3O_4 and Co_3O_4/TiO_2 had similar absorption spectra between 600 nm–800 nm while for pure TiO_2, there are no peaks in this region.[46] Band gap of TiO_2 and $PbTiO_3$ was estimated as 3.1 eV and 2.5 eV, respectively. Similar, to the

^{207}Pb NMR results, increasing Co content did not further change the characteristics of the experimental UV-Vis spectra.

The imaginary part of the dielectric matrix ϵ_2 as a function of the wavelength was calculated for $PbTiO_3$ and Pb_2CoTiO_6 and presented in Fig. 7b. The effect of Co addition to PTO on the main features of absorption spectra agrees with the experimental results. The agreement between the experimental and theory predicted spectra further confirms the double perovskite structure.

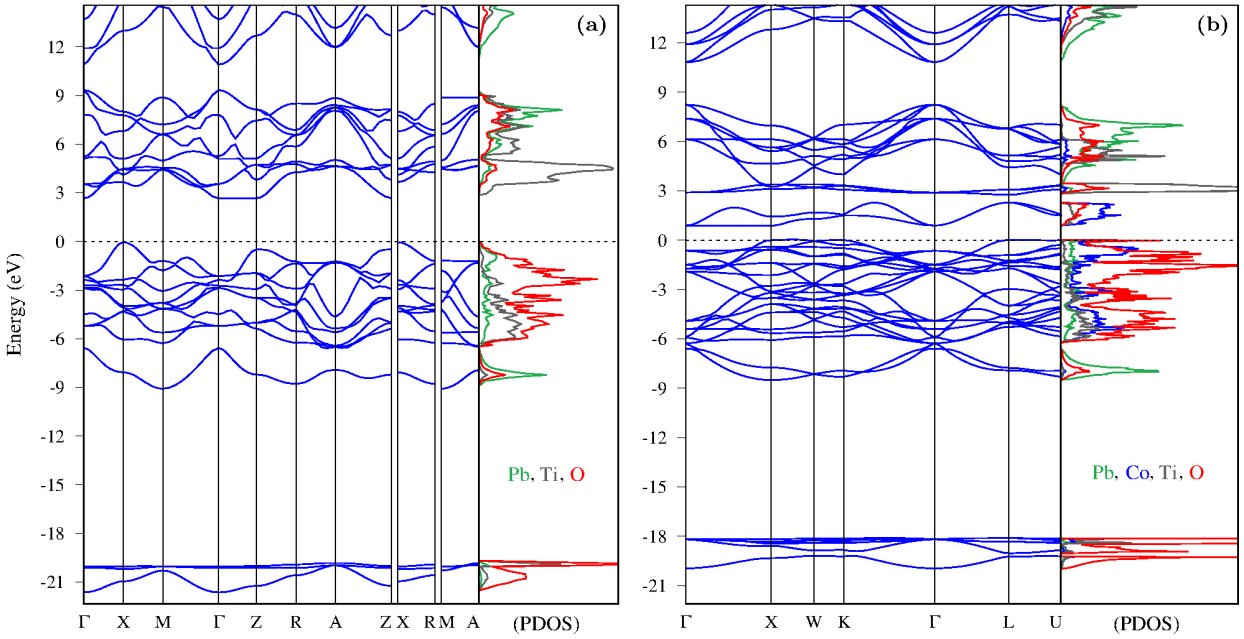

Figure 8: (color on-line) Electronic energy band structures and corresponding projected densities of states (PDOS) of (a) tetragonal $PbTiO_3$ and (b) cubic Pb_2CoTiO_6 calculated using the HSE12s DFT functionals. The zero of the energy eigenvalues are referenced to the Fermi energy which is depicted as dotted lines.

Electronic energy bands and the corresponding partial densities of states (PDOS) are calculated using the HSE functional, for tetragonal $PbTiO_3$ and simple cubic Pb_2CoTiO_6 (See Fig. 8). At first glance, the main features common to perovskites can be seen in both of the materials such as the compositions of core levels, VB, and CB. First of all, the computational method makes a difference in the results. The HSE functional brings a large correction in the band gaps over the standard DFT functionals. For instance, the indirect band gap (XΓ) of $PbTiO_3$ predicted by using the PBE functional is about 1.5 eV and the

width of the valence band (VB) is approximately 8.5 eV. The HSE functional, however, leads to a gap about 2.8 eV in much better agreement with the experiment (2.5 eV) and the VB width is close to 9 eV in Fig. 8a. Pb_2CoTiO_6 is a semiconductor with an indirect band gap (RΓ) of 0.88 eV. The main reason of this drastic difference between the band gaps of pure and Co added $PbTiO_3$ is due to the Co $3d$ driven antibonding t_{2g}–orbitals. These states appear 0.47 eV below the CB as a satellite group which has a width of 1.4 eV.

The bottom of the CB at about 3 eV in Fig. 8b is characterized dominantly by well localized Ti $3d$ t_{2g}-type orbitals. Antibonding states associated with Pb mostly contribute to the upper part of the CB.

The single band in Fig. 8a starting from 0.3 eV below the valence group has a width of 2.6 eV and consists mostly of Pb-6s character. Similarly, in the case of PCTO, a group of bands separated from the bottom of the VB group have the same Pb-6s character. The core level, mostly of O-2s character, is at -20.2 to -21.8 eV in (a), whereas the same bands in (b) are shifted 1.9 eV upward and range from -18.3 to -20.6 eV.

Conclusions

The effects of cobalt incorporation into $PbTiO_3$ perovskites are investigated experimentally as well as by the first principles methods. Consistent with the common expectations, Co replaces lattice Ti. The insertion of cobalt transforms tetragonal $PbTiO_3$ to a cubic Pb_2CoTiO_6 confirmed by XRD, NMR and UV-Vis data as well as their corresponding DFT simulations. The DFT estimated values of ^{207}Pb NMR chemical shift anisotropy tensor components could predict the symmetry around different nuclei with the changes in Co content. NMR lineshape simulations reveal an isotropic structure in addition to the characteristic $PbTiO_3$ lineshape. Based on the DFT investigations, the most probable geometry is found as Pb_2CoTiO_6 which forms in a cubic structure where oxygen and Pb coordination is isotropic. The oxygen vacancy formation energy decreases significantly upon addition of Co as estimated by DFT

in line with the TPR measurements. Co incorporation into the $PbTiO_3$ structure causes a significant narrowing of the band gap as a result of the Co related t_{2g}-type d-states ($\sigma*$) which appear near the bottom of the conduction band.

Acknowledgements

The authors acknowledge the contributions from Dr. Taymaz Tabari and Dr. Jun Xu at the initial phase of this study. Partial financial support for the experimental part of this study was provided by TÜBİTAK under grant no 107M040.

References

(1) Suntivich, J.; Gasteiger, H. A.; Yabuuchi, N.; Nakanishi, H.; Goodenough, J. B.; Shao-Horn, Y. Design principles for oxygen-reduction activity on perovskite oxide catalysts for fuel cells and metal–air batteries. *Nature Chemistry* **2011**, *3*, 546–550.

(2) Chen, Y. Z.; Bovet, N.; Trier, F.; Christensen, D. V.; Qu, F. M.; Andersen, N. H.; Kasama, T.; Zhang, W.; Giraud, R.; Dufouleur, J. et al. A high-mobility two-dimensional electron gas at the spinel/perovskite interface of γ-Al_2O_3/$SrTiO_3$. *Nature Communications* **2013**, *4*, 1371.

(3) Liao, W.-Q.; Zhao, D.; Tang, Y.-Y.; Zhang, Y.; Li, P.-F.; Shi, P.-P.; Chen, X.-G.; You, Y.-M.; Xiong, R.-G. A molecular perovskite solid solution with piezoelectricity stronger than lead zirconate titanate. *Science* **2019**, *363*, 1206–1210.

(4) Spaldin, N. A.; Ramesh, R. Advances in magnetoelectric multiferroics. *Nature Materials* **2019**, *18*, 203–212.

(5) Zhang, S.; Li, F.; Jiang, X.; Kim, J.; Luo, J.; Geng, X. Advantages and challenges of

relaxor-$PbTiO_3$ ferroelectric crystals for electroacoustic transducers - A review. *Progress in Materials Science* **2015**, *68*, 1 – 66.

(6) Erhart, P.; Klein, A.; Åberg, D.; Sadigh, B. Efficacy of the DFT + U formalism for modeling hole polarons in perovskite oxides. *Phys. Rev. B* **2014**, *90*, 035204.

(7) Eichel, R.-A. Structural and dynamic properties of oxygen vacancies in perovskite oxides-analysis of defect chemistry by modern multi-frequency and pulsed EPR techniques. *Phys. Chem. Chem. Phys.* **2011**, *13*, 368–384.

(8) Beck, C. M.; Thomas, N. W.; Thompson, I. Cobalt-doping of lead magnesium niobium titanate: Chemical control of dielectric properties. *Journal of the European Ceramic Society* **1998**, *18*, 1679 – 1684.

(9) Eichel, R.-A. Defect structure of oxide ferroelectrics—valence state, site of incorporation, mechanisms of charge compensation and internal bias fields. *Journal of Electroceramics* **2007**, *19*, 11–23.

(10) Zhou, W.; Deng, H.; Yu, L.; Yang, P.; Chu, J. Optical band-gap narrowing in perovskite ferroelectric ABO_3 ceramics (A=Pb, Ba; B=Ti) by ion substitution technique. *Ceramics International* **2015**, *41*, 13389 – 13392.

(11) Zhou, W.; Deng, H.; Yang, P.; Chu, J. Designing tunable band-gap and magnetization at room-temperature in $Pb(Ti_{1-x}M_x)O_{3-\delta}$ (M=Ni and Pd) thin films. *Materials Letters* **2016**, *185*, 323 – 326.

(12) Li, R.; Zhao, Y.; Li, C. Spatial distribution of active sites on a ferroelectric $PbTiO_3$ photocatalyst for photocatalytic hydrogen production. *Faraday Discuss.* **2017**, *198*, 463–472.

(13) Ahn, C. W.; Borse, P. H.; Kim, J. H.; Kim, J. Y.; Jang, J. S.; Cho, C.-R.; Yoon, J.-H.; seob Lee, B.; Bae, J.-S.; Kim, H. G. et al. Effective charge separation in site-isolated Pt-

nanodot deposited $PbTiO_3$ nanotube arrays for enhanced photoelectrochemical water splitting. *Applied Catalysis B: Environmental* **2018**, *224*, 804 – 809.

(14) Uner, D.; Demirkol, M.; Dernaika, B. A novel catalyst for diesel soot oxidation. *Applied Catalysis B-Environmental* **2005**, *61*, 334–345.

(15) Deml, A. M.; Stevanovic, V.; Muhich, C. L.; Musgrave, C. B.; O'Hayre, R. Oxide enthalpy of formation and band gap energy as accurate descriptors of oxygen vacancy formation energetics. *Energy Environ. Sci.* **2014**, *7*, 1996–2004.

(16) Ermanoski, I.; Siegel, N. P.; Stechel, E. B. A New Reactor Concept for Efficient Solar-Thermochemical Fuel Production. *J. Sol. Energy Eng.* **2013**, *135*, 031002.

(17) Meredig, B.; Wolverton, C. First-principles thermodynamic framework for the evaluation of thermochemical H_2O- or CO_2-splitting materials. *Phys. Rev. B* **2009**, *80*, 245119.

(18) Bykov, I. P.; Zagorodniy, Y. A.; Yurchenko, L. P.; Korduban, A. M.; Nejezchleb, K.; Trachevsky, V. V.; Dimza, V.; Jastrabik, L.; Dejneka, A. Using the methods of radiospectroscopy (EPR, NMR) to study the nature of the defect structure of solid solutions based on lead zirconate titanate (PZT). *IEEE Transactions on Ultrasonics, Ferroelectrics, and Frequency Control* **2014**, *61*, 1379–1385.

(19) Zhao, P.; Prasad, S.; Huang, J.; Fitzgerald, J. J.; Shore, J. S. Lead-207 NMR Spectroscopic Study of Lead-Based Electronic Materials and Related Lead Oxides. *The Journal of Physical Chemistry B* **1999**, *103*, 10617–10626.

(20) Rodriguez-Fortea, A.; Alemany, P.; Ziegler, T. Density Functional Calculations of NMR Chemical Shifts with the Inclusion of Spin-Orbit Coupling in Tungsten and Lead Compounds. *The Journal of Physical Chemistry A* **1999**, *103*, 8288–8294.

(21) Alkan, F.; Dybowski, C. Chemical-shift tensors of heavy nuclei in network solids: a DFT/ZORA investigation of ^{207}Pb chemical-shift tensors using the bond-valence method. *Phys. Chem. Chem. Phys.* **2015**, *17*, 25014–25026.

(22) Kresse, G.; Hafner, J. *Ab initio* molecular dynamics for liquid metals. *Phys. Rev. B* **1993**, *47*, 558–561.

(23) Blöchl, P. E. Projector augmented-wave method. *Phys. Rev. B* **1994**, *50*, 17953–17979.

(24) Kresse, G.; Joubert, D. From ultrasoft pseudopotentials to the projector augmented-wave method. *Phys. Rev. B* **1999**, *59*, 1758–1775.

(25) Heyd, J.; Scuseria, G. E.; Ernzerhof, M. Hybrid functionals based on a screened Coulomb potential. *The Journal of Chemical Physics* **2003**, *118*, 8207–8215.

(26) Paier, J.; Marsman, M.; Hummer, K.; Kresse, G.; Gerber, I. C.; Ángyán, J. G. Erratum: "Screened hybrid density functionals applied to solids" [J. Chem. Phys. 124, 154709 (2006)]. *The Journal of Chemical Physics* **2006**, *125*, 249901.

(27) Paier, J.; Marsman, M.; Hummer, K.; Kresse, G.; Gerber, I. C.; Ángyán, J. G. Screened hybrid density functionals applied to solids. *The Journal of Chemical Physics* **2006**, *124*, 154709.

(28) Umeno, Y.; Meyer, B.; Elsässer, C.; Gumbsch, P. Ab initio study of the critical thickness for ferroelectricity in ultrathin Pt/$PbTiO_3$/Pt films. *Phys. Rev. B* **2006**, *74*, 060101.

(29) Paul, A.; Sun, J.; Perdew, J. P.; Waghmare, U. V. Accuracy of first-principles interatomic interactions and predictions of ferroelectric phase transitions in perovskite oxides: Energy functional and effective Hamiltonian. *Phys. Rev. B* **2017**, *95*, 054111.

(30) Zhang, Y.; Sun, J.; Perdew, J. P.; Wu, X. Comparative first-principles studies of prototypical ferroelectric materials by LDA, GGA, and SCAN meta-GGA. *Phys. Rev. B* **2017**, *96*, 035143.

(31) Bilc, D. I.; Orlando, R.; Shaltaf, R.; Rignanese, G.-M.; Íñiguez, J.; Ghosez, P. Hybrid exchange-correlation functional for accurate prediction of the electronic and structural properties of ferroelectric oxides. *Phys. Rev. B* **2008**, *77*, 165107.

(32) Perdew, J. P.; Burke, K.; Ernzerhof, M. Generalized Gradient Approximation Made Simple. *Phys. Rev. Lett.* **1996**, *77*, 3865–3868.

(33) Perdew, J. P.; Ernzerhof, M.; Burke, K. Rationale for mixing exact exchange with density functional approximations. *The Journal of Chemical Physics* **1996**, *105*, 9982–9985.

(34) Moussa, J. E.; Schultz, P. A.; Chelikowsky, J. R. Analysis of the Heyd-Scuseria-Ernzerhof density functional parameter space. *The Journal of Chemical Physics* **2012**, *136*, 204117.

(35) Weston, L.; Cui, X. Y.; Ringer, S. P.; Stampfl, C. Multiferroic crossover in perovskite oxides. *Phys. Rev. B* **2016**, *93*, 165210.

(36) Weston, L.; Cui, X. Y.; Ringer, S. P.; Stampfl, C. Mechanism for strong magnetoelectric coupling in dilute magnetic ferroelectrics. *Phys. Rev. B* **2016**, *94*, 184419.

(37) Pickard, C. J.; Mauri, F. All-electron magnetic response with pseudopotentials: NMR chemical shifts. *Phys. Rev. B* **2001**, *63*, 245101.

(38) Yates, J. R.; Pickard, C. J.; Mauri, F. Calculation of NMR chemical shifts for extended systems using ultrasoft pseudopotentials. *Phys. Rev. B* **2007**, *76*, 024401.

(39) Gregor, T.; Mauri, F.; Car, R. A comparison of methods for the calculation of NMR chemical shifts. *The Journal of Chemical Physics* **1999**, *111*, 1815–1822.

(40) Sahu, N.; Panigrahi, S.; Kar, M. Structural study of Zr doped $PbTiO_3$ materials by employing Rietveld method. *Advanced Powder Technology* **2011**, *22*, 689–694.

(41) Noheda, B.; Gonzalo, J. A.; Cross, L. E.; Guo, R.; Park, S.-E.; Cox, D. E.; Shirane, G. Tetragonal-to-monoclinic phase transition in a ferroelectric perovskite: The structure of $PbZr_{0.52}Ti_{0.48}O_3$. *Phys. Rev. B* **2000**, *61*, 8687–8695.

(42) Van Bramer, S.; Glatfelter, A.; Bai, S.; Dybowski, C.; Neue, G. Data acquisition and analysis of broad chemical-shift powder patterns from solids with spin–echo techniques. *Concepts in Magnetic Resonance* **2002**, *14*, 365–387.

(43) Ünal, H.; Gülseren, O.; Ellialtıoğlu, Ş.; Mete, E. Electronic structures and optical spectra of thin anatase TiO_2 nanowires through hybrid density functional and quasiparticle calculations. *Phys. Rev. B* **2014**, *89*, 205127.

(44) Choi, J.; Park, H.; Hoffmann, M. R. Effects of Single Metal-Ion Doping on the Visible-Light Photoreactivity of TiO_2. *J. Phys. Chem. C* **2010**, *114*, 783–792.

(45) Deng, S.; Xu, G.; Bai, H.; Li, L.; Jiang, S.; Shen, G.; Han, G. Hydrothermal Synthesis of Single-Crystalline Perovskite PbTiO3 Nanosheets with Dominant (001) Facets. *Inorganic Chemistry* **2014**, *53*, 10937–10943.

(46) Dai, G.; Liu, S.; Liang, Y.; T., L. Synthesis and enhanced photoelectrocatalytic activity of p–n junction Co_3O_4/TiO_2 nanotube arrays. *Appl. Surf. Sci.* **2013**, *264*, 157–161.